

CHEMISTRY

Computer-aided design of reversible hybridization chain reaction (CAD-HCR) enables multiplexed single-cell spatial proteomics imaging

Xiaohao Liu^{1,2†}, Dongsheng Mao^{2,3†}, Yuchen Song², Liucun Zhu², Albertina N. Isak², Cuicui Lu², Guoli Deng², Feng Chen¹, Fenyong Sun^{1*}, Yu Yang^{3*}, Xiaoli Zhu^{1,2*}, Weihong Tan^{3,4,5*}

In situ spatial proteomics analysis of a single cell has not been achieved yet, mainly because of insufficient throughput and sensitivity of current techniques. Recent progress on immuno-nucleic acid amplification technology presents tremendous opportunities to address this issue. Here, we report an innovative hybridization chain reaction (HCR) technique that involves computer-aided design (CAD) and reversible assembly. CAD enables highly multiplexed HCR with a sequence database that can work in parallel, while reversible assembly enables the switching of HCR between a working state and a resting state. Thus, CAD-HCR has been successfully adopted for single-cell spatial proteomics analysis. The fluorescence signal of CAD-HCR is comparable with conventional immunofluorescence, and it is positively correlated with the abundance of target proteins, which is beneficial for the visualization of proteins. The method developed here expands the toolbox of single-cell analysis and proteomics studies, as well as the performance and application of HCR.

INTRODUCTION

Spatial partitioning of proteins within subcellular structures is an essential requirement for cells (1–3). The alteration of subcellular localization of proteins is associated with most cellular processes, such as the relocalization of mitochondrial proteins during apoptosis (4, 5). In addition, mislocalization of proteins involves cellular dysfunction and disease, such as neurodegeneration (6). Research on the localization and quantification of proteins on the subcellular scale belongs to the discipline known as spatial proteomics, a branch of proteomics (7). Now, two methods are available for spatial proteomics analysis: mass spectrometry (MS)–based organelle profiling and imaging-based protein localization approaches (8–11). MS can identify and quantify proteins with high throughput, making it a powerful tool for proteomics research (12–14). On the basis of the separation and enrichment of organelles by subcellular fractionation, MS can be further adopted for spatial proteomics analysis (15). With the progress of quantitative MS in recent years, it is exciting to see that comprehensive, high-resolution organellar maps of single cells have been achieved (16). By coupling with immune recognition, MS has also been used extensively for the analysis of spatial protein–protein interaction networks (17). However, the application of MS in spatial proteomics is not entirely user friendly. It requires cumbersome and intricate steps for organelle separation, especially in a single

cell, and it is unable to provide more high-precision spatial information at the suborganelle level (18–20).

Imaging-based spatial proteomics, on the contrary, has inherent advantages over MS (21). Advancements in superresolution fluorescence microscopy and expansion microscopy have enabled the localization of proteins directly on the subcellular, or even suborganelle, scale (22–24). By using immunofluorescence imaging, Lundberg and colleagues presented a comprehensive and high-resolution map of the subcellular distribution of 12,003 human proteins, providing a valuable resource to deconvolute the highly complex architecture of the human cell (25). It is generally claimed that immunofluorescence imaging is available on the single-cell level. However, a single cell can only be used for the analysis of three to five proteins because of the obvious overlap in excitation and emission spectra of the antibody-conjugated fluorophores (26, 27). Because of the low throughput, immunofluorescence needs a large number of cell samples to achieve spatial proteomics analysis of multiplexed proteins. Therefore, while the traditional immunofluorescence imaging method is unsuited for single-cell analysis, cell-to-cell heterogeneity remains an intrinsic characteristic of most biological systems (28, 29).

Recently, by integrating DNA exchange techniques and immune recognition, Yin and colleagues reported a method named DNA exchange imaging (DEI) and achieved in situ immunofluorescence imaging of multiplexed proteins (30). However, the lack of amplification from secondary antibody results in poor sensitivity, which is not conducive to the imaging of low-abundance targets. Besides, the dependence of DEI on phase correlation–based algorithm and scarce equipment further leads to decreased accessibility. By further introducing signal amplification by exchange reaction (SABER), they also developed an immuno-SABER technique to realize multiplexed and amplified imaging of proteins (31). Although this methodology supports a powerful toolbox for spatial proteomics research, plenty of room remains for improvement in performance. Consider, for example, the contradiction of the need to recruit a large number of amplifiers for signal amplification when their accumulation is likely to be trapped within the cell matrix and glutaraldehyde during the

¹Department of Clinical Laboratory Medicine, Shanghai Tenth People's Hospital, School of Medicine, Tongji University, Shanghai 200072, China. ²Center for Molecular Recognition and Biosensing, School of Life Sciences, Shanghai University, Shanghai 200444, China. ³Institute of Molecular Medicine (IMM), Renji Hospital, Shanghai Jiao Tong University School of Medicine, and College of Chemistry and Chemical Engineering, Shanghai Jiao Tong University, Shanghai 200240, China. ⁴The Cancer Hospital of the University of Chinese Academy of Sciences (Zhejiang Cancer Hospital), Institute of Basic Medicine and Cancer (IBMC), Chinese Academy of Sciences, Hangzhou, Zhejiang 310022, China. ⁵Molecular Science and Biomedicine Laboratory (MBL), State Key Laboratory of Chemo/Biosensing and Chemometrics, College of Chemistry and Chemical Engineering, College of Biology, Aptamer Engineering Center of Hunan Province, Hunan University, Changsha, Hunan 410082, China.

*Corresponding author. Email: sunfenyong@263.net (F.S.); yuyang@shsmu.edu.cn (Y.Y.); xiaolizhu@shu.edu.cn (X.Z.); tan@hnu.edu.cn (W.T.)

†These authors contributed equally to this work.

exchange cycle, causing interference and false signals. Moreover, signal amplification such as SABER is based on a series of long single-stranded sequences, and it is usually not removed during imaging cycles, which may lead to undesirable nonspecific signal. This is especially unfavorable for spatial proteomics that requires precise localization of individual organelles, not just cell membranes, cytoplasm, and nucleus (32). An ideal signal amplification method should be with high sensitivity, specificity, throughput, and accessibility. However, existing technologies have not yet been able to achieve a balance in these aspects.

Here, we report a highly sensitive and multiplexed imaging of proteins within a single cell by integrating the well-established DNA exchange technique with a self-developed high-throughput hybridization chain reaction (HCR). HCR has been recognized as a robust amplification system, and it has been applied for the amplified detection of various targets (33). By conjugating HCR with immune recognition, it has also been applied for the in situ amplified imaging of proteins (34). Here, to adapt HCR to spatial proteomics analysis, progress was made in developing a computer-aided design (CAD) method and creating a sequence database used to construct multiple HCRs that can run independently and simultaneously. In addition, we were able to develop HCR with reversible assembly capability triggered by the target to form aggregates and then disassemble into small building blocks in the presence of an oligonucleotide washer.

RESULTS

CAD of reversible HCR

In a typical HCR, two hairpin oligonucleotides are adopted (35). A single-stranded DNA initiator (abbreviated as “I”) can open one of the hairpins, exposing a previously unidentified single-stranded region that can open the other hairpin (Fig. 1A). The reaction proceeds cyclically, leading to the formation of nicked double-stranded concatemers. Previous reports showed that hundreds to thousands of hairpin building blocks can be assembled (36, 37). To couple HCR with the DNA exchange technique, a reversible HCR is developed here. Two strategies, named gapped HCR (gHCR) and tailed HCR (tHCR), are adopted (Fig. 1B). For gHCR, an extra single-stranded region is inserted in the loop of the first hairpin, while for tHCR, the extra region is placed at the 3′ terminal of the hairpin. After the initiation by an initiator, the two hairpins (namely, H1 and H2) can assemble into double-stranded concatemers with repeated gaps or tails in the case of gHCR and tHCR, respectively (Fig. 1C). To disassemble the concatemers, the extra region (i.e., the gap and tail regions) works as a toehold to bind to an oligonucleotide washer (abbreviated as “W”), which, in turn, can compete with H2 to hybridize with H1 through strand displacement. Thus, the concatemers disassemble such that the initiator is separated from a large number of ternary fragments composed of H1/H2/W.

Next, a database, consisting of H1, H2, I, and W, is created under self-defined rules and by using CAD (Fig. 1D). Four independent regions of the correlated four oligonucleotides, namely, the loop of H2 (region 1), the stem of H1 and H2 (region 2), the loop of tH1 (region 3), and the complementary toehold of W (region 4), are created. The basic design principles of HCR and the division of regions 1, 2, and 3 were referred to traditional HCR, while region 4 was self-defined for the disassembly of the concatemers. On the basis of existing reports on HCR and strand displacement (38–40), the rules are set as follows:

1) Length: The length of region 2 and regions 1, 3, and 4 is set to 16 and 7 nt, respectively.

2) Base composition: The G/C content of region 2 and regions 1, 3, and 4 is fixed at 50% (G/C = 8 nt, A/T = 8 nt) and 43% (G/C = 3 nt, A/T = 4 nt), respectively, to obtain the same thermal stability between multiplexed HCRs.

3) Sequence similarity: The length of any two identical sequences in the database of region 2 and regions 1, 3, and 4 is no more than 6 and 4 nt, respectively, to guarantee that different groups of HCRs can run simultaneously without interfering with each other.

Here, the length of regions was fixed at a medium length used in existing reports, and the content of G/C was fixed at approximately 50% (40 to 60% was commonly used). As for the sequence similarity, it was self-designed and can be modulated. The overall guiding principles are as follows: (i) The capacity of the final database is sufficient for multiplexed imaging (dozens at least), and (ii) cross-reactions among different groups of HCRs are basically eliminated. On the basis of the above rules and by using Perl scripts (the specific codes were attached in the Supplementary Materials and have been deposited on Zenodo), we created a sequence database of region 2 and regions 1, 3, and 4, in which 174 sequences are allotted for region 2 (table S2) and 208 sequences for regions 1, 3, and 4 (table S3). Thus, by randomly selecting the sequences in the database to compose H1, H2, I, and W, gHCR and tHCR can be established. Theoretically, the sequence database can support 103 gHCRs or tHCRs to work simultaneously in the 208 sequences for regions 1, 3, and 4: 208 divided by 2 for regions 1 and 3 each, leaving 2 for unified region 4. Note that the capacity of the sequence database can be expanded or reduced by modifying the design rules as needed. For example, increasing sequence similarity can expand the sequence database, but cross-reactions among multiplexed HCRs can occur in the case of high similarity of sequences. Therefore, a balance between similarity and cross-reactions should be taken into account.

By conjugating with immune recognition, the reversible multiplexed gHCR or tHCR is expected to be available for spatial proteomics analysis. The specific workflow is illustrated in Fig. 1E. In detail, initiators that can orthogonally launch multiplexed gHCR or tHCR are labeled on a specific primary antibody (abbreviated as “PA”). All the “3n” initiator-barcoded primary antibodies are applied to the cells simultaneously to barcode the target proteins (abbreviated as “P”) with orthogonal initiators. Then, the cells are ready for imaging cycles. In the first imaging cycle, three of the 3n initiators labeled on the target-bound primary antibodies orthogonally launch three independent gHCRs or tHCRs labeled with red-, green-, and yellow-colored fluorophores, respectively. Thus, in situ amplified imaging analysis of three proteins is achieved. After adding orthogonal washers, the HCR concatemers are expected to disassemble into fragments, leaving only the initiator-barcoded primary antibodies on the cells. Then, the second imaging cycle is ready to be conducted by using another three gHCRs or tHCRs, which are orthogonal to the corresponding target proteins and so as to avoid interference from residual nonorthogonal initiators. After “n” cycles, $3 \times n$ proteins can be imaged through $3 \times n$ groups of gHCRs or tHCRs. Last, by recoloring and aligning these images generated through several cycles by a computer, one comprehensive image with subcellular localization of a large number of proteins within a single cell can be obtained.

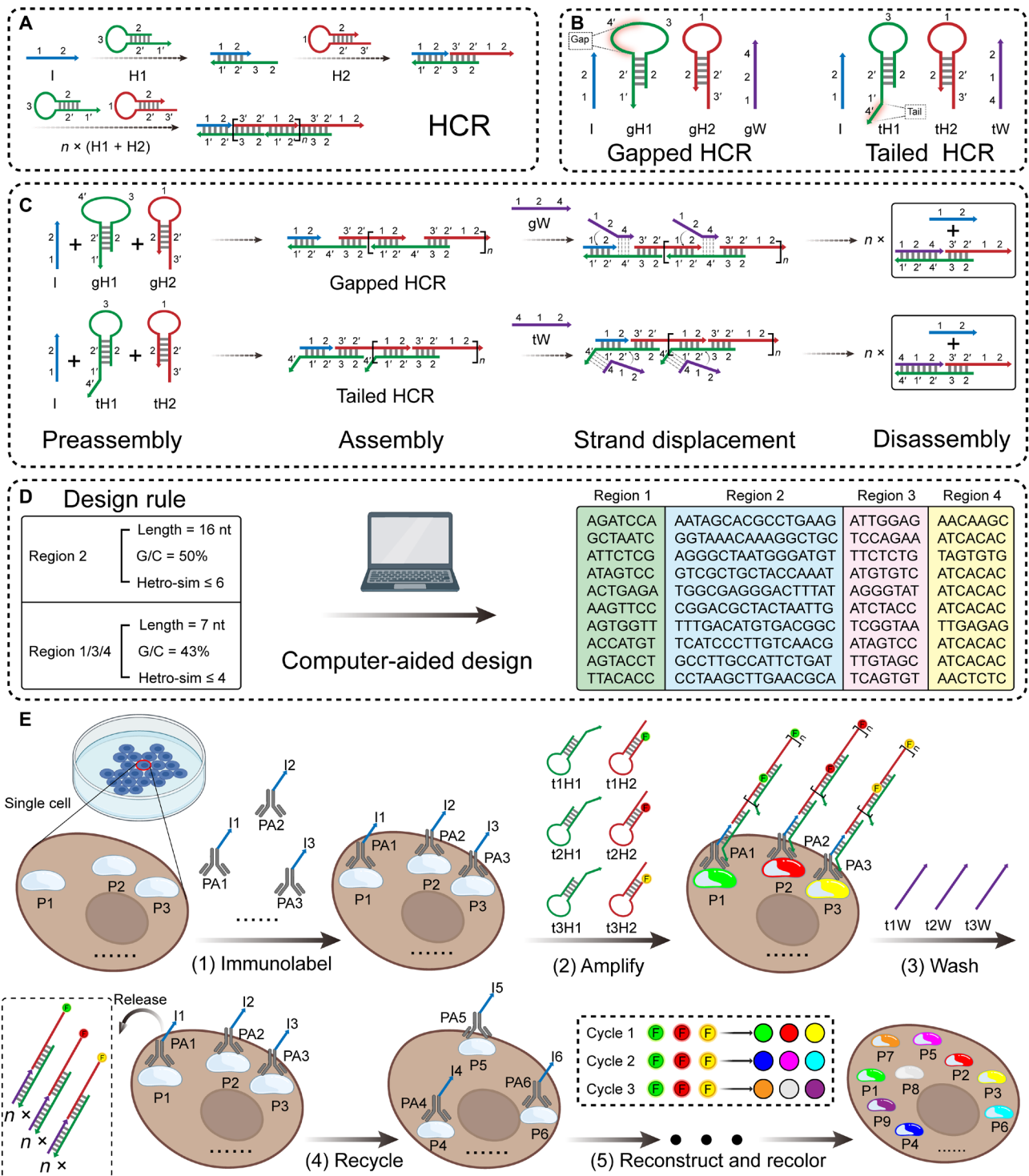


Fig. 1. Overview of reversible multiplexed gHCR and tHCR and their application for spatial proteomics imaging analysis. (A) Schematic of conventional HCR. (B) Detailed information of the building blocks of gHCR and tHCR. (C) Assembly and disassembly of gHCR and tHCR. (D) Overview of the CAD of multiplexed gHCR and tHCR. (E) Workflow of the application of tHCR for spatial proteomics imaging analysis.

Characterization of reversible HCR in vitro

Ten groups of gHCRs and tHCRs (table S1) were established, respectively, as a model by randomly selecting 10 groups of H1, H2, I, and W from the sequence database. Agarose gel electrophoresis was

adopted to study the assembly and disassembly of gHCR and tHCR. In the case of tHCR, Fig. 2A shows that the corresponding tH1 and tH2 form double-stranded amplified concatemers in the presence of orthogonal initiators (the second lane of each group),

while clear bands of the tH1 and tH2 monomers can be observed in the absence of initiators (the first lane of each group). Adding washer to the assembled tH1 and tH2 further causes the disassembly of the concatemers and the formation of ternary fragments composed of tH1/tH2/tW (the third lane of each group), which appears as clear bands with a larger molecular weight than the monomers. Similar results are also obtained in the case of gHCR, suggesting that both of them can work as expected in vitro (Fig. 2B). Figure 2 (C and D) and fig. S1 show that only the orthogonal initiators can trigger the corresponding HCR, while other initiators are totally invalid. Note that H1 and H2 are indistinguishable in the electrophoresis, because they have similar length and composition, while for I, its band is missing, because the shorter length, lower concentration, and single-stranded structure make it difficult to be stained and visualized. Furthermore, the thermal stability of the desired domain and undesired domain between initiators and hairpins was verified through

Nucleic Acid Package (NUPACK) (fig. S2). Results show that the free energy of all the desired domains is approximately -29 kcal/mol, while the free energy of all undesired domains varies between -12 and 0 kcal/mol. The significant difference in free energy is considered to be the main factor that limits cross-reactions, and it should be attributed to the rational design rules. The results lay the foundation for parallel work of multiplexed HCR, which should benefit from CAD and the avoidance of mutual interference caused by the sequence similarity.

The reversible and orthogonal assembly of tHCR and gHCR was also confirmed by using atomic force microscopy (AFM), allowing the products of amplified concatemers and disassembled fragments to be clearly observed as long linear strands with a typical height of double strands (41, 42) and punctate distribution, respectively (Fig. 2, E and F, and figs. S3 and S4). By labeling t1H1, g1H1, t3H1, g3H1, t1H2/g1H2, and t3H2/g3H2 with a quencher [Black Hole

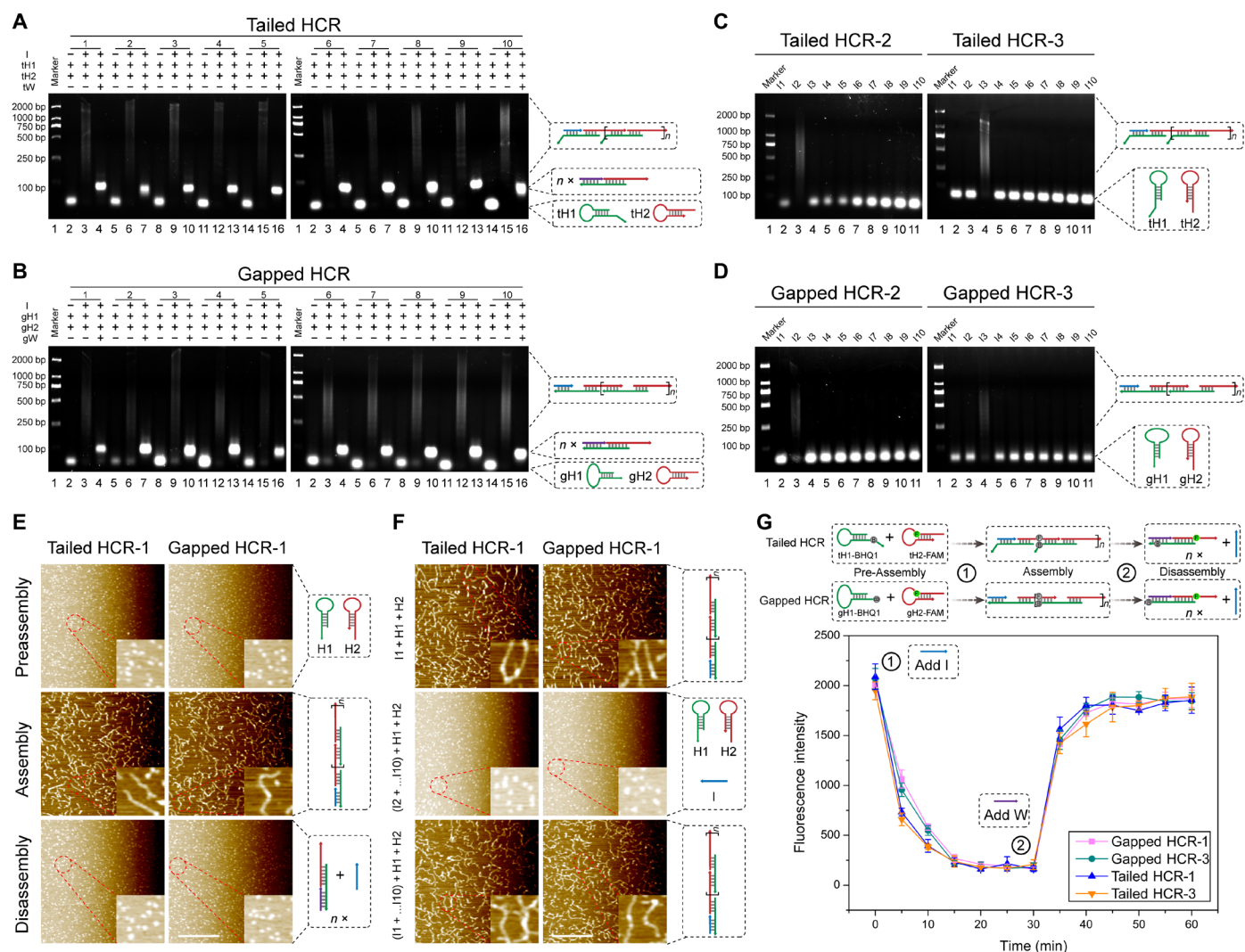


Fig. 2. Characterization of tHCR and gHCR in vitro. (A and B) Agarose gel analysis of the assembly and disassembly of 10 groups of (A) tHCR and (B) gHCR. (C and D) Agarose gel analysis of the orthogonality of two groups of (C) tHCR and (D) gHCR. (E) Atomic force microscopy (AFM) images of the products of tHCR and gHCR (one group each) before assembly, after assembly and after disassembly. (F) AFM images of the products of tHCR and gHCR (one group each) initiated by different initiators. (G) Dynamic fluorescence analysis of the assembly and disassembly of the two groups of tHCR and gHCR. The data represent the means \pm SD (error bars) of triplicate experiments. Scale bars, 500 nm.

Quencher 1 (BHQ1) at the 3' terminus of region 1' of H1] and a fluorophore [Carboxyfluorescein (FAM) at the 3' terminus of region 2' of H2], respectively, the dynamics of the reversible assembly of tHCR and gHCR were further studied. Figure 2G shows that the assembly progresses after the initiator is added. As that happens, the proximity of H1 and H2 forces the measured fluorescence to gradually decrease over time and reach equilibrium within 30 min, indicating that the assembly was completed. After adding the washer, fluorescence gradually recovers within 30 min, suggesting the complete disassembly of the concatemers. Note that different groups of tHCR and gHCR show unexpected consistency in dynamics, mainly from consistent sequence length and composition of each region, as specified in the CAD rules. Compared with gHCR and tHCR, traditional HCR with the same regions 1, 2, and 3 exhibits similar assembly dynamics, but it cannot be disassembled without region 4, i.e., the "tail" or the "gap" (fig. S5) (34). Dynamics study based on fluorescent labeling further confirmed the orthogonality of tHCR and gHCR (fig. S6). Last, we show that both tHCR and gHCR have good universality in different buffer systems and favorable stability over time (fig. S7). Together, the above results demonstrate that both tHCR and gHCR can work well in vitro.

Feasibility of reversible HCR for in situ imaging

We next investigated the feasibility of reversible HCR for spatial proteomics imaging by conjugating the HCR with immune recognition. PA-DNA conjugates were synthesized using a chemical cross-linker [sulfo-succinimidyl-4-(*N*-maleimidomethyl) cyclohexane-1-carboxylate (sulfo-SMCC)], following the workflow shown in fig. S8A. The conjugation was analyzed by SDS-polyacrylamide gel electrophoresis (SDS-PAGE) stained with Coomassie brilliant blue, and the successful conjugation was confirmed by observing a small shift in the apparent molecular weights of the primary antibody (β -actin) after its conjunction with the DNA initiator (fig. S8B). The PA-DNA conjugation ratio was calculated to be ca. 1:2 by labeling the initiator with a fluorophore and measuring the fluorescence intensity of the conjugates after separation through ultrafiltration (fig. S9).

The PA-DNA conjugates were then adopted for fluorescence imaging. Results show that all the nine prepared conjugates could be used for conventional immunofluorescence analysis, suggesting that the primary antibody maintained activity and immunogenicity with high specificity and affinity (Fig. 3A and fig. S10). In parallel, the DNA initiator of the conjugates maintained its activity to initiate HCR, presenting an amplified in situ fluorescence imaging signal of cellular proteins (Fig. 3B). Colocalization studies show that the reversible HCR can be well colocalized with immunofluorescence, demonstrating a good specificity of the reversible HCR (fig. S11). However, note that the fluorescence distribution of reversible HCR results slightly differs from immunofluorescence results, which should be attributed to the deviation caused by the large products. Briefly, there is a trade-off between the signal amplification generated by DNA aggregation and the fidelity of imaging: Larger aggregates can produce better signal amplification but, at the same time, lead to the deviation of imaging. This is also a common challenge for aggregate-based signal amplification technologies (HCR, rolling circle amplification, SABER, etc.) and should be addressed by introducing other innovative concepts.

Further results also show that both tHCR and gHCR had good orthogonality for in situ fluorescence imaging (Fig. 3C). Only the orthogonal initiator triggered the corresponding HCR and outputting

fluorescence imaging signal. To simultaneously analyze multiple proteins within a single imaging cycle, three fluorophores with distinctive excitation (Ex) and emission (Em) wavelengths were used (FAM: Ex/Em = 494/518 nm, Cy3: Ex/Em = 552/570 nm, and Cy5: Ex/Em = 643/667 nm; Fig. 3D). By comparing independent imaging (Fig. 3E) and simultaneous imaging (Fig. 3F), we can see that the localization and fluorescence intensity of the targeted proteins dovetail nicely with each other (Fig. 3G), suggesting that these three fluorophores do not interfere with each other and are available for simultaneous imaging. The good orthogonality should be attributed to the lowest possible sequence similarity between different groups of HCRs in the CAD. Cross-reaction of reversible HCRs with high sequence similarity [approximately 80% sequence similarity: 5/7 nt (similarity = 71.4%) for regions 1, 3, and 4 and 13/16 nt (similarity = 81.2%) for region 2] was adopted as a comparison to verify the importance of sequence similarity design rules in CAD. As expected, significant cross-reactions emerged (fig. S12), which caused serious confusion in the imaging results. Notably, the similarity of some sequences used in the previously reported immuno-SABER is as high as 8/10 nt (80%) (31), which is inevitable without CAD and would result in cross-reactions.

Comparison of amplification folds

The amplification effect of reversible HCR was further studied. First, one of the two HCR hairpins (H2) was modified with a fluorescent dye for amplification effect verification. As shown in Fig. 4, for the imaging analysis of four independent proteins, including β -actin, Ezrin, voltage-dependent anion channel (VDAC), and α -tubulin, both tHCR and gHCR enhance the fluorescence signal by approximately 65-fold in comparison with the unamplified group. The fluorescence signal of both tHCR and gHCR is comparable with conventional immunofluorescence, which is conducive to subsequent imaging. Moreover, by modifying both HCR hairpins (H1 and H2) with a fluorescent dye, additional signal amplification can be achieved, indicating the expandability of reversible HCR in the amplification efficiency (fig. S13). The quantitative performance of the reversible HCR was further studied. As described in our previous study, Michigan Cancer Foundation-7 (MCF-7) cells treated with benzyl- α -*N*-acetylgalactosamine (GalNAc), a specific inhibitor of Mucin 1 (MUC1), were investigated (43). As shown in fig. S14, there is a positive correlation between protein abundance and fluorescence intensity of reversible HCR when the target protein expression was altered, which is consistent with existing reports (44). Although the assembly degree of a single HCR is generally considered to be beyond precise control, the results here show that the reversible HCR can be used in the semiquantitative analysis of target proteins. Besides, with the development of HCR technology, a method to control the assembly degree of HCR through the introduction of a base-pair mismatch in the duplex of the hairpins has recently been reported (45), which may improve the performance of the quantification of HCR.

Study on the reversibility of CAD-HCR

We next investigated the ability of reversible HCR for expanded multiplexed imaging. To achieve this goal, a prerequisite should be met. That is, after each staining and imaging cycle, the fluorophore-labeled HCR concatemers must be thoroughly washed to avoid a residual fluorescence signal in the subsequent cycles. Two groups of tHCR (tHCR-1 and tHCR-2) were adopted for cyclic imaging of two target proteins (β -actin and Ezrin) (Fig. 5A). During the 10 cycles,

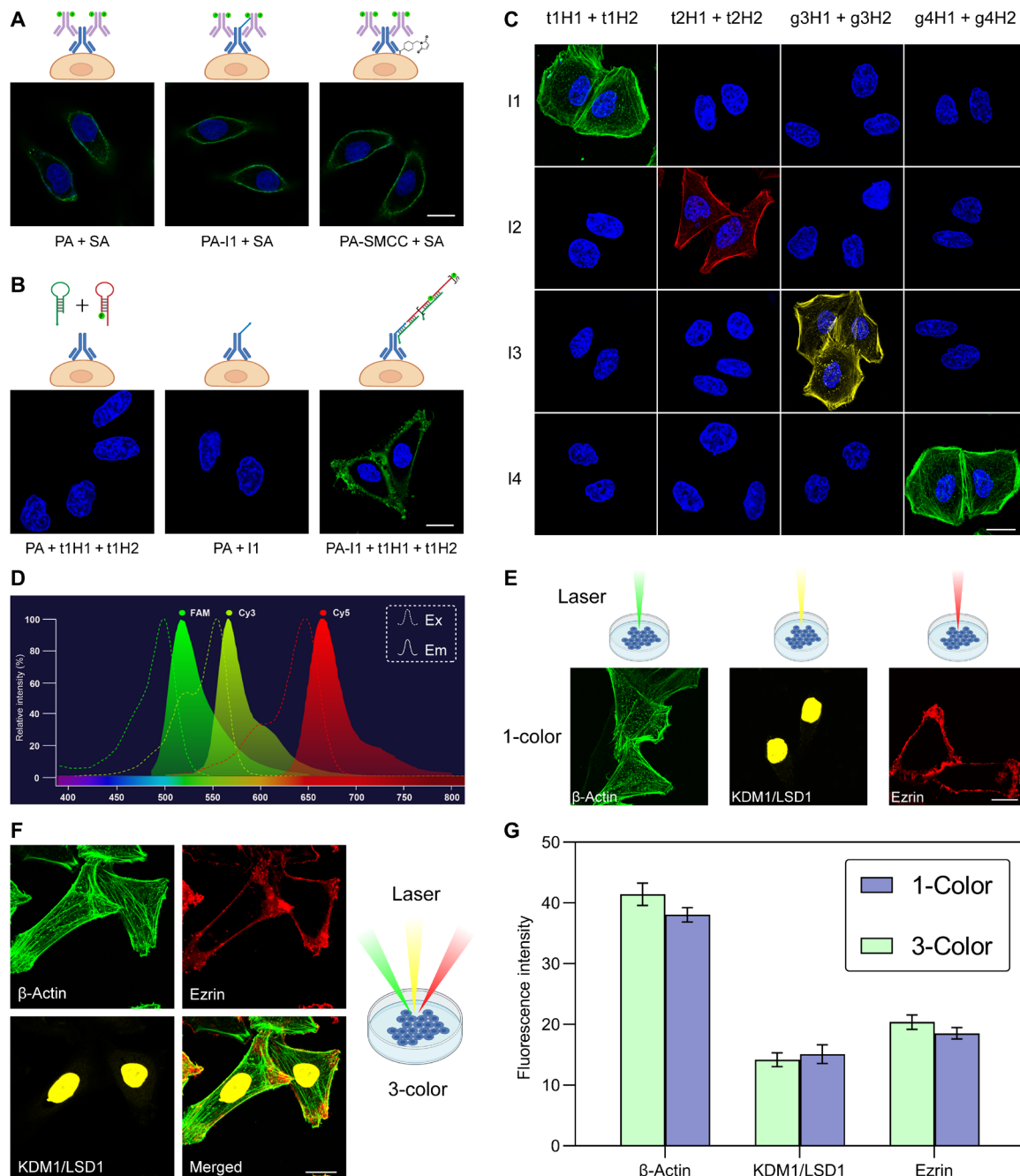


Fig. 3. Feasibility of reversible HCR for in situ imaging. (A) Conventional immunofluorescence of Ezrin on HeLa cells. The primary antibody was either used as is, labeled with the initiator (I1), or modified with the cross-linker (sulfo-SMCC). Alexa Fluor 488–modified secondary antibody (SA) was adopted for imaging. (B) Imaging of Ezrin on HeLa cells using I1 and its corresponding orthogonal t1H1 and t1H2 (labeled with FAM) was adopted. In the control groups, either the initiator or both t1H1 and t1H2 were absent. (C) Orthogonal imaging of β -actin on HeLa cells using tHCR and gHCR. Two groups of tHCR and gHCR each were adopted. (D) Excitation (Ex) and emission (Em) spectra of FAM, Cy3, and Cy5. (E) One-color staining image of β -actin (tHCR-1 and FAM), Ezrin (tHCR-2 and Cy5), and KDM1/LSD1 (tHCR-3 and Cy3) on HeLa cells. (F) Three-color staining image of β -actin (tHCR-1 and FAM), Ezrin (tHCR-2 and Cy5), and KDM1/LSD1 (tHCR-3 and Cy3) on HeLa cells. (G) Statistical results of fluorescence intensity from (E) and (F) by ImageJ software. The data represent the means \pm SD (error bars) of fluorescence intensity between different regions on the same sample. Scale bars, 20 μ m.

the imaging results show almost identical staining patterns, suggesting that the staining and destaining cycles were achieved without affecting the cell's morphology (Fig. 5B). Quantitative analysis of the fluorescence intensity from Fig. 5B also shows stable signal outputs during the cycles, demonstrating that the antigenicity of the

primary antibodies and the hybridizability of the initiators were also unaffected (Fig. 5, C to E). The stable signal output during the cycles demonstrates that the overall signal is controllable when the reaction time is strictly controlled (36, 46). The reversible HCR is speculated to endow samples with high reusability by eliminating

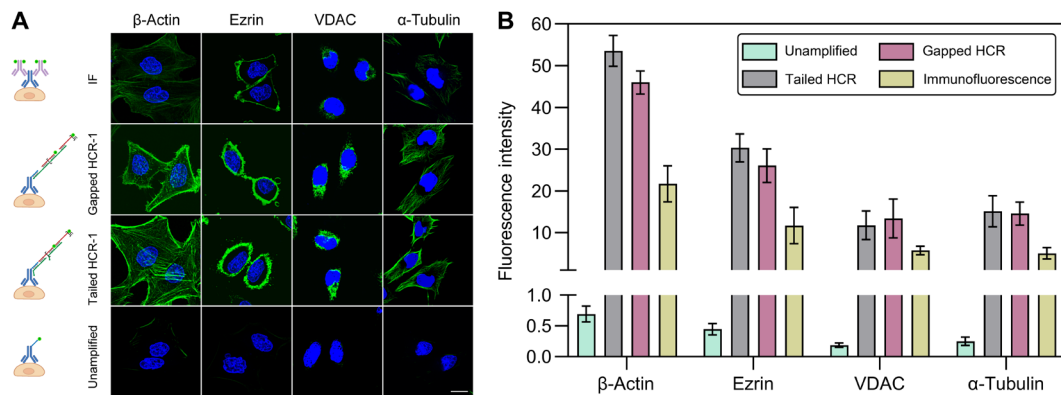


Fig. 4. Amplified imaging using reversible HCR by modifying H2 with a fluorescent dye. (A) Confocal laser scanning microscope images of β -actin, Ezrin, VDAC, and α -tubulin on HeLa cells by using unamplified, gHCR, tHCR, and conventional immunofluorescence (IF). (B) Quantitative bar plots analyzed by ImageJ software of the fluorescence intensity of the images shown in (A). The data represent the means \pm SD (error bars) of fluorescence intensity between different regions on the same sample. Scale bar, 20 μ m.

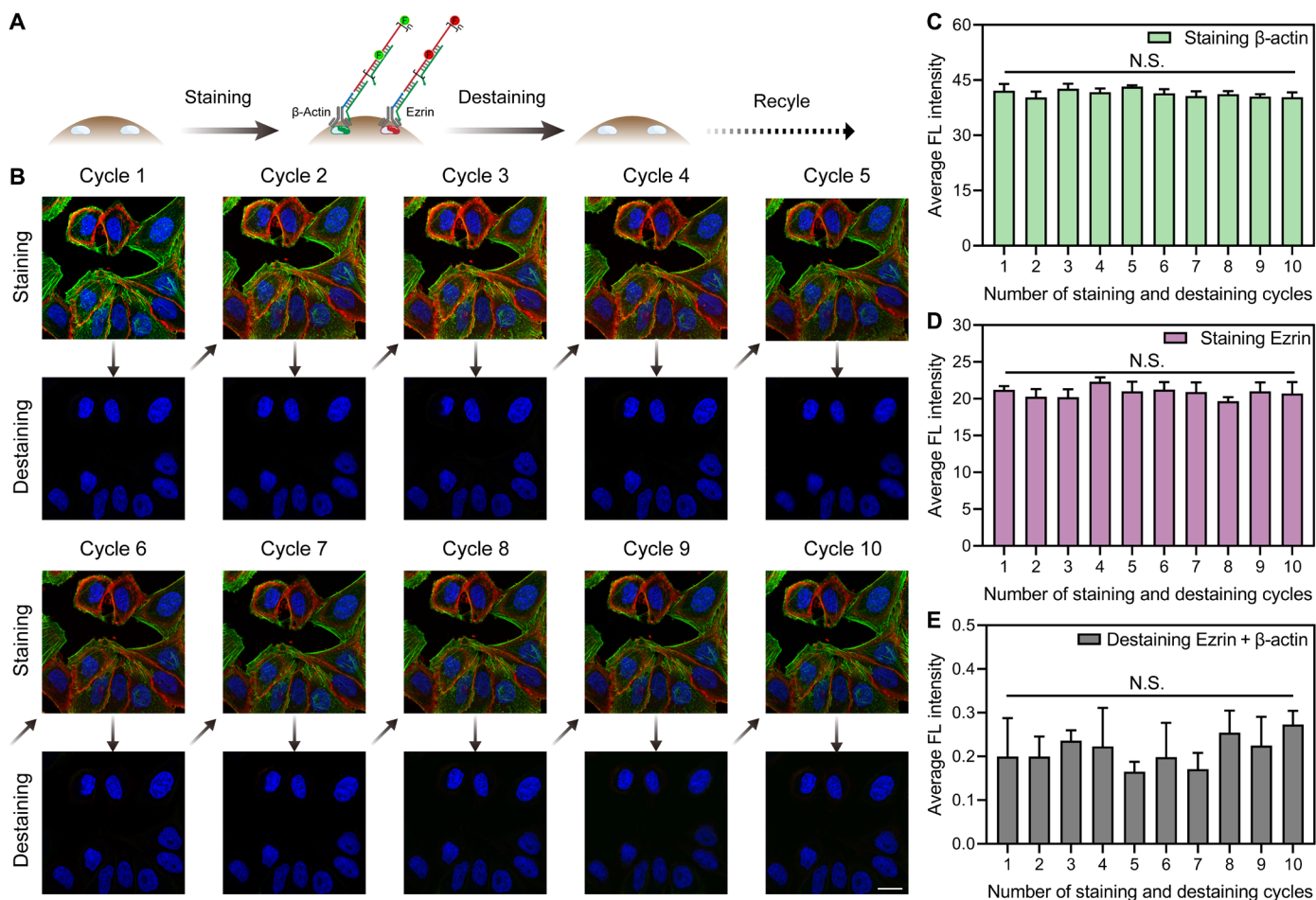


Fig. 5. Cyclic staining and destaining via reversible HCR. (A) Schematic diagram of cyclic staining and destaining. (B) Confocal laser scanning microscope images of 10 staining and destaining cycles. tHCR-1 and tHCR-2 were adopted for cyclic imaging of β -actin (green) and Ezrin (red), respectively. HeLa cells were stained with 4',6-diamidino-2-phenylindole (DAPI) (blue). (C to E) Statistical results of fluorescence intensity from the images of (B). Data represent the means \pm SD (error bars) of fluorescence intensity between different regions on the same sample. N.S., no significance. Scale bar, 20 μ m.

irreversible signal attenuation, which is unachieved by traditional immunofluorescence technology. It is valuable in various practical applications, especially for the repeated analysis of precious clinical samples and experimental samples (exosomes, cells, tissues, protein chips, etc.) over a long period of time.

CAD-HCR assisted spatial proteomics imaging within a single cell

Last, by using reversible HCR, we performed multiplexed imaging of nine proteins distributed in different subcellular locations within a single cell. The proteins include Ezrin (a plasma membrane marker), β -actin (a cytoskeleton marker), α -tubulin (a cytoskeleton marker), Golgi matrix 130 (GM130) (a cis-Golgi marker), VDAC (a mitochondrial outer membrane marker), lamin B1 (a nuclear envelope marker), Lysine-specific demethylase 1 (KDM1/LSD1) (a nuclear marker), Sirtuin-1 (SIRT1) (a nuclear marker), and Fibrillarin like 1 (FBLL1) (a nucleolar marker). The presence of these nine proteins in a HeLa cell was first confirmed by Western blot (fig. S15). As shown above, 10 orthogonal systems were verified experimentally, and 9 of the 10 orthogonal

HCRs were used here to image the nine proteins within three cycles. As shown in Fig. 6A, the nine proteins were divided into three groups, and the three proteins in each group were imaged by using three groups of orthogonal tHCR labeled with FAM (green), Cy3 (yellow), and Cy5 (red), respectively. It should be noted here that the same set of three orthogonal HCRs cannot be reused in the imaging cycles, because after each imaging cycle, the antibody-initiator DNA conjugates cannot be washed away and they would initiate the corresponding orthogonal HCR in the next cycle if the same set of three orthogonal HCRs are applied, resulting in false outputting signals. Figure 6B shows the separate fluorescent images of the nine proteins after three cycles of imaging, which can be reconstructed and recolored to obtain an integrated image (Fig. 6C). A single cell circled in a red dashed line in Fig. 6C is also shown in Fig. 6D, layer by layer, to display the localization of each protein. As shown, the distribution of the nine proteins matches well with their theoretical location. In particular, note that the results of multiplexed imaging of the subcellular proteins colocalized well with the subcellular locations, showing the high accuracy of reversible HCR in the spatial localization of proteins

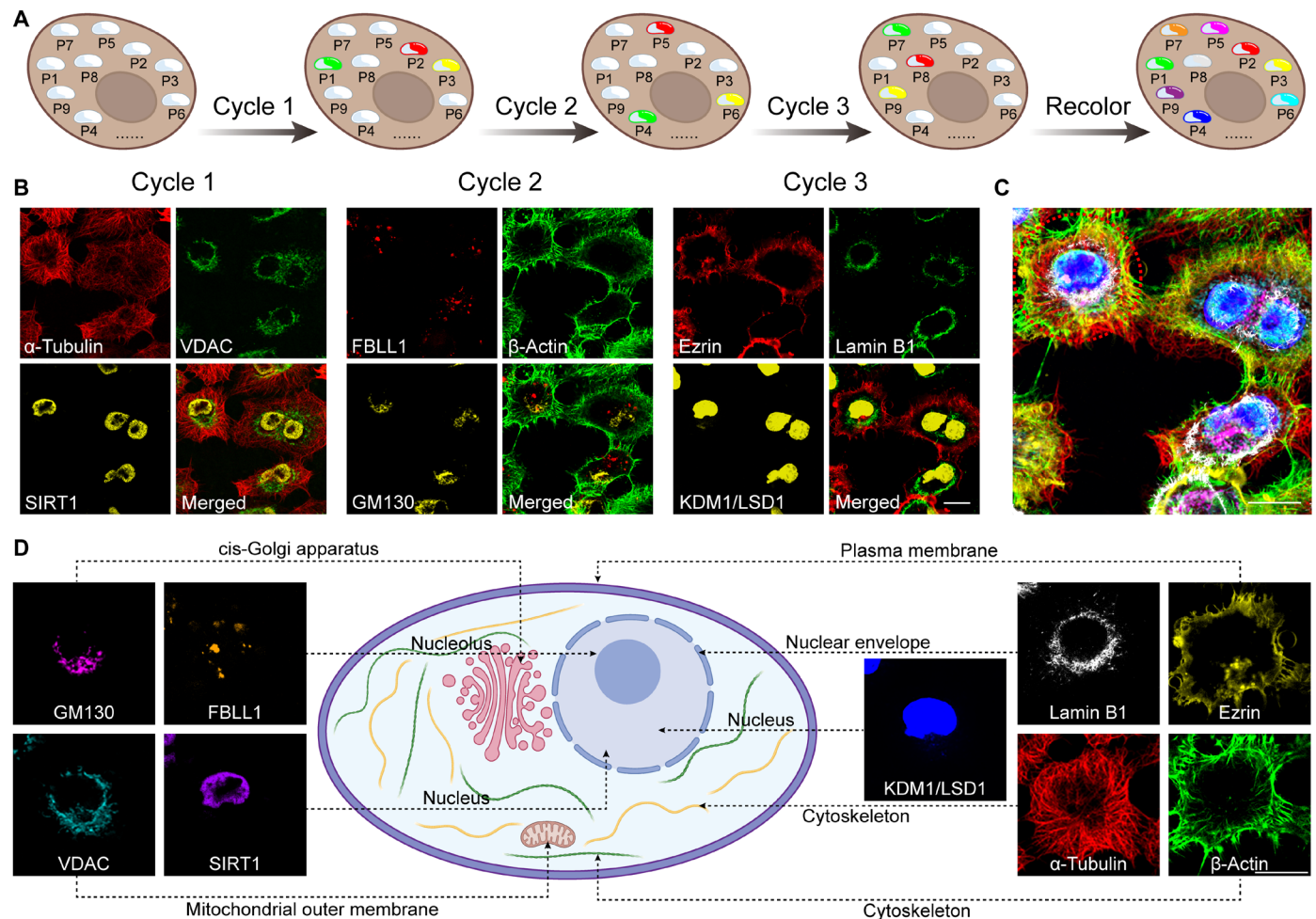


Fig. 6. Multiplexed staining of nine proteins within a single cell. (A) Schematic diagram of cyclic imaging of nine proteins in a single cell. (B) Confocal laser scanning microscope images of the nine proteins through three imaging cycles. The first cycle: VDAC (tHCR-1 and FAM), α -tubulin (tHCR-2 and Cy5), and SIRT1 (tHCR-3 and Cy3); the second cycle: β -actin (tHCR-4 and FAM), FBLL1 (tHCR-5 and Cy5), and GM130 (tHCR-6 and Cy3); and the third cycle: lamin B1 (tHCR-7 and FAM), Ezrin (tHCR-8 and Cy5), and KDM1/LSD1 (tHCR-9 and Cy3). (C) A reconstructed false-color image from (B). (D) The location of each protein in a single cell circled in a red dashed line in (C). Scale bars, 20 μ m.

at subcellular scales (fig. S16). The performance of gHCRs was also studied in the spatial proteomics imaging within a single cell. As shown in fig. S17, similar imaging performance of gHCRs to tHCRs is obtained, indicating that both the tHCR and gHCR can be applied to proteomics imaging in a single cell. By simply changing the primary antibody-DNA conjugates, this reversible HCR can be extended to cyclic imaging and multiplexed imaging of other proteins. In the era of single-cell analysis and omics analysis, reversible HCR-assisted proteomics analysis is considered important for research on the field of cell signaling, protein-protein interaction networks, and precious disease diagnosis. Besides, owing to the mildness of the reaction system, this reversible HCR could be extended to the analysis of membrane proteins in living cells.

DISCUSSION

In summary, benefiting from CAD, we have developed a multiplexed and reversible HCR that can be triggered by orthogonal initiators to form concatemers and disassemble into fragments in the presence of washers. By conjugating with immune recognition, this innovative HCR system was successfully applied to sensitive imaging analysis of spatial proteomics at the single-cell level. CAD enables the construction of a scalable sequence database for multiplexed HCRs that can work in parallel, while reversible tHCR and gHCR make cyclic imaging of multiplexed proteins on a single cell possible. Compared with conventional immunofluorescence, reversible HCR enables efficient signal amplification and can provide comparable fluorescence signal intensity. Besides, we demonstrated that the fluorescence intensity of CAD-HCR is positively correlated with the abundance of protein. So, benefiting from the efficient signal amplification and sensitive responsiveness of CAD-HCR, semi-quantitative and subcellular localization of target proteins can be achieved through a conventional laser confocal microscope, which is more accessible for most laboratories and test centers. By further integrating CAD-HCR with superresolution fluorescence microscopy, single-molecule imaging is considered achievable (30). In addition, the imaging cycles can be repeated at least 10 times without signal passivation and cell deformation. Imaging analysis of nine proteins distributed in various subcellular locations through three imaging cycles was thereby achieved. The method developed here enriches the toolbox of single-cell analysis and proteomics analysis. Looking forward, it has the expanded potential for application in clinical diagnostics and biomedical research.

Despite great efforts, there are still some limitations in our study. First, the method is expected to be extended to other omics-related studies, chip analysis, liquid biopsy of complex systems, etc., but it is not explored in this paper. In addition, there is a trade-off between the degree of signal amplification and imaging fidelity. An orthogonal system labeled with highly fluorescent probes, e.g., quantum dots, can lead to better imaging results and is expected to improve the imaging fidelity of subcellular localization of target proteins. However, more in-depth research is still needed. Last, we hope to further optimize the overall experimental procedure and apply it in clinical sample detection.

MATERIALS AND METHODS

Materials and reagents

All DNA oligonucleotides were synthesized by Sangon Biotech Co. Ltd. (Shanghai, China) and purified by high-performance liquid

chromatography. All DNA sequences used in this paper are listed in table S1. Five times loading buffer with GelRed was purchased from Shanghai Generay Biotech Co. Ltd. (China). DNA Ladder [100 base pairs (bp)] was purchased from Vazyme Biotech Co. Ltd. (Nanjing, China). Mica slice was purchased from Yunfeng Co. Ltd. (China). Benzyl- α -GalNAc was purchased from Sigma-Aldrich. Paraformaldehyde (PFA) (4%) was purchased from BBI Life Sciences Corporation (Shanghai, China). Immunostaining permeabilization buffer with saponin and 4',6-diamidino-2-phenylindole (DAPI) were purchased from Beyotime Biotechnology (Shanghai, China). Bovine serum albumin (BSA) (10%) was purchased from Shanghai ZCIBIO Technology Co. Ltd. (China). Laser confocal glass-bottomed dishes (catalog number: 801001) were purchased from NEST Biotechnology Co. Ltd. (Wuxi, China). Sulfo-SMCC, dithiothreitol (DTT), 10K Molecular Weight Cut Off (MWCO) Zeba Spin Desalting Column, and 3K MWCO Zeba Spin Desalting Column were obtained from Thermo Fisher Scientific Co. Ltd. (Shanghai, China). RIPA (radioimmunoprecipitation assay) lysis buffer, prestained color protein ladder (6.5 to 270 kDa), Coomassie blue fast staining solution, PDVF (polyvinylidene fluoride) membranes, PMSF (phenylmethanesulfonyl fluoride), and 5 \times SDS-PAGE sample loading buffer were purchased from Beyotime Biotechnology (Shanghai, China). ECL Western Blotting Substrate was purchased from Beijing Solarbio Science and Technology Co. Ltd. (China). All antibodies were purchased from Abcam (Cambridge, UK), Biosynthesis Biotechnology Inc. (Beijing, China), Sino Biological Inc. (Beijing, China), and Sangon Biotech Co. Ltd. (Shanghai, China). The detailed product name, supplier, and catalog number (Cat. No.) are listed in table S4. HeLa and MCF-7 cells were obtained from the Cell Bank of the Chinese Academy of Sciences (Shanghai, China). Dulbecco's modified Eagle's medium (DMEM), fetal bovine serum (FBS), antibiotics (penicillin-streptomycin-nystatin solution), and 0.25% EDTA-trypsin were purchased from Biological Industries (Beit Haemek, Israel). LiveCyte DMSO (dimethyl sulfoxide)-free was purchased from Beijing T&L Biological Technology Co. Ltd. (China). 1,1'-Diiodo-3,3',3'-Tetramethylindodicarbocyanine,4-Chlorobenzenesulfonate Salt (DiI), MitoRed, and Golgi-Tracker Red were purchased from Jiangsu KeyGEN BioTECH Co. Ltd. (China). Other reagents were analytical grade at least and were used as received.

Gel electrophoresis analysis

Agarose gel electrophoresis was performed for the analysis of the tHCR and gHCR products. A volume of 4 μ l of the samples was mixed with 1 μ l of 5 \times loading buffer with GelRed and added to a 2% agarose gel. One hundred-base pair DNA Ladder was used as a marker.

The electrophoresis experiments were conducted in 1 \times Tris-Acetic acid-EDTA (TAE) at 120 V for 30 min. The imaging of the gel was performed using a Gel Doc XR Imaging System (Bio-Rad, USA).

Atomic force microscopy

Morphological characterization of assembly and disassembly of tHCR and gHCR was carried out using AFM. Ten-microliter samples (1:1 diluted by 20 mM magnesium chloride) were spread onto a freshly cleaved mica slice, followed by 30-s incubation at room temperature (RT). The mica slice was then washed with double-distilled water and dried with nitrogen immediately following AFM imaging. All AFM images were acquired using an Agilent 5500 AFM (Agilent Technologies) in tapping mode. NSC-15/Al BS tips with a nominal spring constant of 40 N m⁻¹ and a resonant frequency of approximately 325 kHz were used.

Fluorescence measurements

The fluorescence spectra of FAM, Cy3, and Cy5 were collected at a maximal excitation wavelength of 494, 552, and 643 nm. The peak fluorescence at 518, 570, and 667 nm was recorded for quantification. Dynamic fluorescence analysis of the assembly and disassembly of traditional HCR, tHCR, and gHCR were performed at RT. The concentrations of H1, FAM-labeled H2, I, and W were 500, 500, 100, and 500 nM, respectively. The changes in fluorescence intensity were recorded at an interval of 5 min (Ex: 494 nm; Em: 518 nm). All fluorescence measurements were carried out using an F-7000 fluorescence spectrophotometer (Hitachi, Japan).

Immunofluorescence

HeLa cells were collected at the end of the log phase and seeded in laser confocal glass-bottomed dishes at a density of 1×10^4 cells/ml in a total volume of 1 ml, followed by an incubation step at 37°C for 24 hours for better cell attachment. The cells were fixed in 4% PFA for 20 min at RT and washed three times with phosphate-buffered saline (PBS) for 5 min each, permeabilized in immunostaining permeabilization buffer with saponin for 10 min at RT, rewashed three times with PBS for 5 min each, and blocked with 1% BSA, glycine (22.52 mg/ml) in PBST (PBS + 0.1% Tween 20) for 1 hour at RT. After being washed three times with PBS for 5 min each, the cells were incubated overnight at 4°C with the primary antibodies diluted in PBST containing 1% BSA, followed by washing three times with PBS for 5 min each. The cells were then incubated with fluorophore-conjugated secondary antibodies in 1% BSA for 1 hour at RT in the dark, washed with PBS, and then stained with DAPI for 15 min at RT. After being washed three times with PBS for 5 min each, the cells were imaged using the LSM 710 confocal laser scanning microscope (Zeiss, Germany).

Conjunction of DNA and primary antibody

Primary antibodies were suspended in reaction buffer [55 mM sodium phosphate, 150 mM sodium chloride, and 20 mM EDTA (pH 7.2)], followed by a 2-hour incubation of 80-fold excess of sulfo-SMCC (dissolved in anhydrous DMSO) at RT to activate the amino group of primary antibodies. A 10K MWCO Zeba spin desalting column was used to separate out redundant sulfo-SMCC by centrifuge ultrafiltration for three rounds. In parallel, we reduced the thiol-modified initiators with DTT at a molar ratio of 1:500 in the reaction buffer for 1 hour at 37°C. Excess DTT in the thiolated DNA solution was removed by a 3K MWCO Zeba spin desalting column. The sulfo-SMCC-activated primary antibodies were mixed with a threefold molar excess of reduced initiators and reacted at RT for 2 hours. The conjugation was verified by 8% native SDS-PAGE. After electrophoresis, the gel was visualized by Coomassie brilliant blue staining. The specific staining methods were carried out according to the manufacturer's instructions. Last, protein-DNA conjugates were further purified by the 10K MWCO Zeba Spin Desalting Column and stored at 4°C for short-term usage or at -20°C until used.

Cyclic staining and destaining

All oligonucleotides were dissolved in PBS to 100 μ M and stored at -20°C. Before use, 10 μ M stock solution was heated to 95°C for 5 min to denature and then cooled slowly to RT to form the specific structure in PBS. As described in the "Immunofluorescence" section, HeLa cells were fixed, permeabilized, and blocked in turn. Then, the HeLa cells were stained with DAPI for 15 min at RT. After being

washed three times with PBS for 5 min each, two initiator-conjugated primary antibodies (anti- β -actin antibody, 1:1000; anti-Ezrin antibody, 1:500) diluted in PBST containing 1% BSA were simultaneously incubated with cells overnight at 4°C. After being washed with PBS, two groups of H1 and H2 (500 nM) were added and incubated at 37°C for 1 hour in the dark to complete the HCR. The cells were washed with PBS and imaged using a confocal laser scanning microscope to obtain the "staining" photos. After adding orthogonal washers (500 nM) for 30 min at RT, the HCR concatemers were disassembled into fragments. After another washing step, "destaining" photos were imaged under a confocal laser scanning microscope. Thus, the first cycle of in situ amplified cyclic staining and destaining imaging was over. Subsequently, the next cycle of staining and destaining could be conducted by repeating the step from "adding two groups of H1 and H2" to the step of "obtaining the destaining photos" expected for the DAPI staining.

Multiplexed staining of nine proteins

As described in the "Cyclic staining and destaining" section, all oligonucleotides were heated and annealed. HeLa cells were fixed, permeabilized, and blocked in turn. Then, nine initiator-conjugated primary antibodies diluted in PBST containing 1% BSA were simultaneously incubated with cells overnight at 4°C (the detailed dilution rate was shown in table S4), followed by washing to remove the unspecific binding. Thus, the cells are ready for imaging cycles. First, three groups of H1 and H2 (500 nM) were added and incubated at 37°C for 1 hour in the dark. The cells were washed with PBS and imaged using a confocal laser scanning microscope. After adding orthogonal washers (500 nM) for 30 min at RT, the HCR concatemers were disassembled into fragments, followed by a washing step. Thus, the first in situ amplified imaging cycle of three proteins was finished. For the second imaging cycle, another three groups of H1 and H2 were added and incubated with HeLa cells. Then, the cells were washed with PBS and imaged. After adding orthogonal washers, followed by a washing step, the second imaging cycle of another three proteins was achieved. The third imaging cycle process was the same as the second imaging cycle. Last, one integrated image with subcellular localization of nine proteins within a single cell could be obtained by recoloring and aligning the fluorescent images generated through three cycles.

Western blot analysis

HeLa cells were seeded and cultured in a six-well plate. At the end of the growth log phase, the cells were washed with ice-cold PBS, lysed in RIPA lysis buffer containing 1% PMSF on ice for 30 min, and then centrifuged at 15,000g for 15 min at 4°C. The supernatants were collected in tubes and diluted in 5 \times SDS-PAGE sample loading buffer and boiled for 10 min at 100°C. Ten microliters of the samples was separated by SDS-PAGE gel, 80 V for the time samples were running in the stacking gel, and 110 V for the remaining time, followed by electrotransfer onto PDVF membranes. The membranes were blocked with 2% (w/v) BSA in PBST for 1 hour at RT and incubated with primary antibody at 4°C overnight. After being washed three times with PBST for 5 min each, the membranes were incubated with a secondary antibody conjugated with HRP (horseradish peroxidase) for 60 min at RT, followed by protein visualization with the ECL Western Blotting Substrate detected by a ChemiDoc XRS Plus luminescent image analyzer (Bio-Rad, USA).

Cell culture

HeLa cells were grown in DMEM supplemented with 10% FBS, penicillin (100 U/ml), streptomycin (100 µg/ml), and nystatin (12.5 U/ml) and cultured in a humidified atmosphere of 5% CO₂ at 37°C. Cells were suspended in LiveCyte DMSO-free, immersed in liquid nitrogen for long-term storage, and collected at the end of the log phase for the following experiments.

Statistical analysis

Fluorescence intensity was analyzed using ImageJ software. The statistical analysis was performed using one-way analysis of variance (ANOVA) by GraphPad Prism (GraphPad Software, La Jolla, CA). Results were presented as means ± SD.

SUPPLEMENTARY MATERIALS

Supplementary material for this article is available at <https://science.org/doi/10.1126/sciadv.abk0133>

[View/request a protocol for this paper from Bio-protocol.](#)

REFERENCES AND NOTES

- L. M. Orre, M. Vestlerlund, Y. Pan, T. Arslan, Y. Zhu, A. Fernandez Woodbridge, O. Frings, E. Fredlund, J. Lehtio, SubCellBarCode: Proteome-wide mapping of protein localization and relocalization. *Mol. Cell* **73**, 166–182.e7 (2019).
- P. J. Thul, C. Lindskog, The human protein atlas: A spatial map of the human proteome. *Protein Sci.* **27**, 233–244 (2018).
- O. M. Crook, C. M. Mulvey, P. D. W. Kirk, K. S. Lilley, L. Gatto, A Bayesian mixture modelling approach for spatial proteomics. *PLoS Comput. Biol.* **14**, e1006516 (2018).
- A. Digre, C. Lindskog, The Human Protein Atlas—Spatial localization of the human proteome in health and disease. *Protein Sci.* **30**, 218–233 (2021).
- S. Pankow, S. Martínez-Bartolomé, C. Bamberger, J. R. Yates, Understanding molecular mechanisms of disease through spatial proteomics. *Curr. Opin. Chem. Biol.* **48**, 19–25 (2019).
- C. M. Guardia, R. De Pace, R. Mattera, J. S. Bonifacino, Neuronal functions of adaptor complexes involved in protein sorting. *Curr. Opin. Neurobiol.* **51**, 103–110 (2018).
- E. Lundberg, G. H. H. Borner, Spatial proteomics: A powerful discovery tool for cell biology. *Nat. Rev. Mol. Cell Biol.* **20**, 285–302 (2019).
- G. H. H. Borner, Spatial Proteomics: A gateway to understanding cell biology. *Proteomics* **20**, 1900328 (2020).
- J. E. Keener, G. Zhang, M. T. Marty, Native mass spectrometry of membrane proteins. *Anal. Chem.* **93**, 583–597 (2021).
- M. Lu, C. F. Kaminski, G. S. K. Schierle, Advanced fluorescence imaging of in situ protein aggregation. *Phys. Biol.* **17**, 021001 (2020).
- S. Wang, F. Ji, Z. Li, M. Xue, Fluorescence imaging-based methods for single-cell protein analysis. *Anal. Bioanal. Chem.* **411**, 4339–4347 (2019).
- R. Aebersold, M. Mann, Mass-spectrometric exploration of proteome structure and function. *Nature* **537**, 347–355 (2016).
- E. J. Lanni, S. S. Rubakhin, J. V. Sweedler, Mass spectrometry imaging and profiling of single cells. *J. Proteomics* **75**, 5036–5051 (2012).
- E. Reading, Structural mass spectrometry of membrane proteins within their native lipid environments. *Chemistry* **24**, 13391–13398 (2018).
- D. N. Itzhak, C. Davies, S. Tyanova, A. Mishra, J. Williamson, R. Antrobus, J. Cox, M. P. Weekes, G. H. H. Borner, A mass spectrometry-based approach for mapping protein subcellular localization reveals the spatial proteome of mouse primary neurons. *Cell Rep.* **20**, 2706–2718 (2017).
- M. Bantscheff, M. Schirle, G. Sweetman, J. Rick, B. Kuster, Quantitative mass spectrometry in proteomics: A critical review. *Anal. Bioanal. Chem.* **389**, 1017–1031 (2007).
- L. C. M. Mackinder, C. Chen, R. D. Leib, W. Patena, S. R. Blum, M. Rodman, S. Ramundo, C. M. Adams, M. C. Jonikas, A spatial interactome reveals the protein organization of the Algal CO₂-concentrating mechanism. *Cell* **171**, 133–147.e14 (2017).
- B. Dornon, R. Aebersold, Mass spectrometry and protein analysis. *Science* **312**, 212–217 (2006).
- I. Mikšik, Coupling of CE-MS for protein and peptide analysis. *J. Sep. Sci.* **42**, 385–397 (2019).
- J. Han, H. Permentier, R. Bischoff, G. Groothuis, A. Casini, P. Horvathovich, Imaging of protein distribution in tissues using mass spectrometry: An interdisciplinary challenge. *Trac Trends Anal. Chem.* **112**, 13–28 (2019).
- K. Chughtai, R. M. A. Heeren, Mass spectrometric imaging for biomedical tissue analysis. *Chem. Rev.* **110**, 3237–3277 (2010).
- F. Chen, P. W. Tillberg, E. S. Boyden, Expansion microscopy. *Science* **347**, 543–548 (2015).
- R. Yan, B. Wang, K. Xu, Functional super-resolution microscopy of the cell. *Curr. Opin. Chem. Biol.* **51**, 92–97 (2019).
- E. L. Faulkner, S. G. Thomas, R. K. Neely, An introduction to the methodology of expansion microscopy. *Int. J. Biochem. Cell Biol.* **124**, 105764 (2020).
- P. J. Thul, L. Åkesson, M. Wiking, D. Mahdessian, A. Geladaki, H. A. Blal, T. Alm, A. Asplund, L. Björk, L. M. Breckels, A. Bäckström, F. Danielsson, L. Fagerberg, J. Fall, L. Gatto, C. Gnann, S. Hober, M. Hjelmare, F. Johansson, S. Lee, C. Lindskog, J. Mulder, C. M. Mulvey, P. Nilsson, P. Oksvold, J. Rockberg, R. Schutten, J. M. Schwenk, Å. Sivertsson, E. Sjöstedt, M. Skogs, C. Stadler, D. P. Sullivan, H. Tegel, C. Winsnes, C. Zhang, M. Zwahlen, A. Mardinoglu, F. Pontén, K. von Feilitzen, K. S. Lilley, M. Uhlén, E. Lundberg, A subcellular map of the human proteome. *Science* **356**, eaal3321 (2017).
- Y. Goltsev, N. Samusik, J. Kennedy-Darling, S. Bhate, M. Hale, G. Vazquez, S. Black, G. P. Nolan, Deep profiling of mouse splenic architecture with codex multiplexed imaging. *Cell* **174**, 968–981.e15 (2018).
- J.-R. Lin, M. Fallahi-Sichani, P. K. Sorger, Highly multiplexed imaging of single cells using a high-throughput cyclic immunofluorescence method. *Nat. Commun.* **6**, 8390 (2015).
- J. P. Junker, A. van Oudenaarden, Every cell is special: Genome-wide studies add a new dimension to single-cell biology. *Cell* **157**, 8–11 (2014).
- S. Waldherr, Estimation methods for heterogeneous cell population models in systems biology. *J. R. Soc. Interface* **15**, 20180530 (2018).
- Y. Wang, J. B. Woehrstein, N. Donoghue, M. Dai, M. S. Avendaño, R. C. J. Schackmann, J. J. Zoeller, S. S. H. Wang, P. W. Tillberg, D. Park, S. W. Lapan, E. S. Boyden, J. S. Brugge, P. S. Kaeser, G. M. Church, S. S. Agasti, R. Jungmann, P. Yin, Rapid sequential in situ multiplexing with DNA exchange imaging in neuronal cells and tissues. *Nano Lett.* **17**, 6131–6139 (2017).
- S. K. Saka, Y. Wang, J. Y. Kishi, A. Zhu, Y. Zeng, W. Xie, K. Kirli, C. Yapp, M. Cicconet, B. J. Beliveau, S. W. Lapan, S. Yin, E. S. Boyden, P. S. Kaeser, G. Pihan, G. M. Church, P. Yin, Immuno-SABER enables highly multiplexed and amplified protein imaging in tissues. *Nat. Biotechnol.* **37**, 1080–1090 (2019).
- M. Uhlén, L. Fagerberg, B. M. Hallström, C. Lindskog, P. Oksvold, A. Mardinoglu, Å. Sivertsson, C. Kampf, E. Sjöstedt, A. Asplund, I. Olsson, K. Edlund, E. Lundberg, S. Navani, C. A.-K. Szgyarto, J. Odeberg, D. Djureinovic, J. O. Takanen, S. Hober, T. Alm, P.-H. Edqvist, H. Berling, H. Tegel, J. Mulder, J. Rockberg, P. Nilsson, J. M. Schwenk, M. Hamsten, K. von Feilitzen, M. Forsberg, L. Persson, F. Johansson, M. Zwahlen, G. von Heijne, J. Nielsen, F. Pontén, Tissue-based map of the human proteome. *Science* **347**, 1260419 (2015).
- Y. Zhao, F. Chen, Q. Li, L. Wang, C. Fan, Isothermal amplification of nucleic acids. *Chem. Rev.* **115**, 12491–12545 (2015).
- R. Lin, Q. Feng, P. Li, P. Zhou, R. Wang, Z. Liu, Z. Wang, X. Qi, N. Tang, F. Shao, M. Luo, A hybridization-chain-reaction-based method for amplifying immunosignals. *Nat. Methods* **15**, 275–278 (2018).
- R. M. Dirks, N. A. Pierce, Triggered amplification by hybridization chain reaction. *Proc. Natl. Acad. Sci. U.S.A.* **101**, 15275–15278 (2004).
- H. M. T. Choi, J. Y. Chang, L. A. Trinh, J. E. Padilla, S. E. Fraser, N. A. Pierce, Programmable in situ amplification for multiplexed imaging of mRNA expression. *Nat. Biotechnol.* **28**, 1208–1212 (2010).
- H. Chu, J. Zhao, Y. Mi, Y. Zhao, L. Li, Near-infrared light-initiated hybridization chain reaction for spatially and temporally resolved signal amplification. *Angew. Chem. Int. Ed.* **58**, 14877–14881 (2019).
- H. Bui, V. Miao, S. Garg, R. Mokhtar, T. Song, J. Reif, Design and analysis of localized DNA hybridization chain reactions. *Small* **13**, 1602983 (2017).
- Y. S. Ang, L.-Y. L. Yung, Rational design of hybridization chain reaction monomers for robust signal amplification. *Chem. Commun.* **52**, 4219–4222 (2016).
- H. Bui, S. Garg, V. Miao, T. Song, R. Mokhtar, J. Reif, Design and analysis of linear cascade DNA hybridization chain reactions using DNA hairpins. *New J. Phys.* **19**, 015006 (2017).
- S. Zhang, C. Chen, C. Xue, D. Chang, H. Xu, B. J. Salena, Y. Li, Z.-S. Wu, Ribbon of DNA lattice on gold nanoparticles for selective drug delivery to cancer tissues. *Angew. Chem. Int. Ed.* **59**, 14584–14592 (2020).
- D. Mao, T. Chen, X. Liu, L. Ren, C. Feng, G. Chen, A proximity-exponential hybridization chain reaction (PEHCR) and its application for nondestructive analysis of membrane protein-protein interactions on living cells. *Anal. Chim. Acta* **1125**, 8–18 (2020).
- X. Liu, D. Mao, G. Deng, Y. Song, F. Zhang, S. Yang, G. Li, F. Liu, W. Cao, X. Zhu, Nondestructive analysis of tumor-associated membrane protein MUC1 in living cells based on dual-terminal amplification of a DNA ternary complex. *Theranostics* **10**, 4410–4421 (2020).
- D. Yang, Y. Tang, P. Miao, Hybridization chain reaction directed DNA superstructures assembly for biosensing applications. *Trac Trends Anal. Chem.* **94**, 1–13 (2017).
- C. A. Figg, P. H. Winegar, O. G. Hayes, C. A. Mirkin, Controlling the DNA hybridization chain reaction. *J. Am. Chem. Soc.* **142**, 8596–8601 (2020).
- Z. Wu, G.-Q. Liu, X.-L. Yang, J.-H. Jiang, Electrostatic nucleic acid nanoassembly enables hybridization chain reaction in living cells for ultrasensitive mRNA imaging. *J. Am. Chem. Soc.* **137**, 6829–6836 (2015).

Acknowledgments: We thank the members of the laboratory for feedback and discussions. We also thank D. Chu for code support. **Funding:** This work was supported by the National Natural Science Foundation of China under grant nos. 22074090, 81930066, 81772941, and 22107065 and the Natural Science Foundation of Shanghai under grant no. 19ZR1474200. **Author contributions:** W.T., X.Z., Y.Y., and F.S. conceived the concept. X.Z., X.L., D.M., and C.L. designed the experiments. X.L., D.M., Y.S., C.L., and G.D. carried out the extracellular experiments. X.L., Y.S., and A.N.I. carried out the cell experiments. L.Z., X.Z., D.M., and X.L. designed and implemented the CAD-HCR. X.Z., X.L., and D.M. analyzed the data. W.T., X.Z., X.L., D.M., F.C., Y.Y., and F.S. wrote, reviewed, and edited the paper. All authors contributed to the final text of the paper. **Competing interests:** The authors

declare that they have no competing interests. **Data and materials availability:** All data needed to evaluate the conclusions in the paper are present in the paper and/or the Supplementary Materials. The specific codes have been deposited on Zenodo (<http://doi.org/10.5281/zenodo.5520160>).

Submitted 16 June 2021

Accepted 22 November 2021

Published 14 January 2022

10.1126/sciadv.abk0133